Composite Structures 113 (2014) 328–338

Contents lists available at ScienceDirect

Composite Structures

journal homepage: www.elsevier.com/locate/compstruct

Dynamic stability analysis of carbon nanotube-reinforced functionally graded cylindrical panels using the element-free kp-Ritz method

Z.X. Lei [a,b], L.W. Zhang [c], K.M. Liew [b,d,*], J.L. Yu [a]

[a] CAS Key Laboratory of Mechanical Behavior and Design of Materials, University of Science and Technology of China, PR China
[b] Department of Civil and Architectural Engineering, City University of Hong Kong, Kowloon, Hong Kong
[c] College of Information Technology, Shanghai Ocean University, 999 Huchenghuan Road, Shanghai 201306, PR China
[d] City University of Hong Kong Shenzhen Research Institute Building, Shenzhen Hi-Tech Industrial Park, Nanshan District, Shenzhen, PR China

ARTICLE INFO

Article history:
Available online 26 March 2014

Keywords:
Functionally graded materials
kp-Ritz method
Panels
Dynamic stability

ABSTRACT

In this paper, a first-known dynamic stability analysis of carbon nanotube-reinforced functionally graded (CNTR-FG) cylindrical panels under static and periodic axial force by using the mesh-free *kp*-Ritz method is presented. The cylindrical panels are reinforced by single-walled carbon nanotubes (SWCNTs) with different types of distributions, i.e. uniform and three kinds of functionally graded distributions of carbon nanotubes along thickness direction of the panels. Eshelby–Mori–Tanaka approach is employed to estimate effective material properties of the resulting nanocomposite panels. By applying the Ritz minimization procedure to the energy expressions, a system of Mathieu–Hill equations is formulated. Then the principal instability regions are analyzed through Bolotin's first approximation. Detailed parametric studies have been carried out to reveal the influences of volume fraction of carbon nanotubes, edge-to-radius ratio and radius-to-thickness ratio. In addition, effects of different boundary conditions and types of distributions of carbon nanotubes are examined in detail.

1. Introduction

The dynamic stability or phenomenon of parametric resonance in cylindrical shells under periodic loads has drawn considerable attention from researchers due to its detrimental and destabilizing effects in many engineering applications. The investigation about this phenomenon in elastic systems was first studied by Bolotin [1], who found the dynamic instability regions. Vijayaraghavan and Evan-Iwanowski [2] analytically and experimentally studied parametric instability of thin, circular cylindrical shells subjected to in-plane longitudinal inertia loading arising from sinusoidal base excitation. Srinivasan and Chellapandi [3] investigated dynamic stability of laminated rectangular plates due to periodic in-plane load. Moorthy and Reddy [4] studied the parametric instability of plates with transverse shear deformation under uniaxial, harmonically-varying, in-plane loads.

Based on the modified Donnell equations, which included the transverse inertia force, Nagai and Yamaki [5] examined the dynamic stability of circular cylindrical shells under both static and periodic compressive forces, using Hsu's method for different boundary conditions. By using a perturbation technique, Argento and Scott [6,7] studied the dynamic stability of layered anisotropic circular cylindrical shells under axial loading. The dynamic stability of stiffened isotropic and laminated composite plates and shells was studied based on a finite element model with a 3-D degenerated shell element and a 3-D degenerated curved beam element by Liao and Cheng [8]. Ng et al. [9] reported the dynamic stability of cross-ply laminated composite cylindrical shells under combined static and periodical axial forces using Love's classical thin shell theory. Ganapathi and Balamurugan [10] studied the dynamic instability of laminated composite circular cylindrical shells subjected to periodic load, using a C° shear flexible two-node axisymmetric shell element. Park and Kim [11] analyzed the dynamic stability of a completely free isotropic circular cylindrical shell under a follower force.

Motivated by the concept of functionally graded materials [12,13], the pattern of the functionally graded distribution of reinforcement has been successfully applied for carbon nanotube-reinforced functionally graded (CNTR-FG) cylindrical panels. Based on the first order shear deformation plate theory, Zhu et al. [14] carried out bending and free vibration analyses of functionally graded carbon nanotube reinforced composite plates using the finite element method. Employing a two-step perturbation technique, Shen [15] reported an analysis of nonlinear bending of functionally graded CNTRC plates in thermal environments. Based

* Corresponding author. Tel.: +852 34426581.
E-mail address: kmliew@cityu.edu.hk (K.M. Liew).

http://dx.doi.org/10.1016/j.compstruct.2014.03.035
0263-8223/

on Timoshenko beam theory and von Kármán geometric nonlinearity, Ke et al. [16] examined nonlinear free vibration responses of functionally graded nanocomposite beams. Based on three-dimensional theory of elasticity, Alibeigloo [17] studied bending behavior of functionally graded carbon nanotube reinforced composite plate embedded in thin piezoelectric layers subjected to mechanical uniform load with simply supported boundary conditions. With the same theory, a further study about bending behavior of functionally graded carbon nanotube-reinforced composite rectangular plate subjected to thermo-mechanical loads was carried out [18]. By using the mesh-free *kp*-Ritz, Lei et al. [19] investigated post-buckling behaviors of carbon nanotube-reinforced functionally graded cylindrical panels. Alibeigloo [20] examined free vibration behavior of functionally graded carbon nanotube reinforced composite cylindrical panel embedded in piezoelectric layers with simply supported boundary conditions. Shen and Xiang [21] studied the large amplitude vibration behavior of nanocomposite cylindrical shells in thermal environments, by using a mesh-free method. Moradi-Dastjerdi et al. [22] presented a dynamic analysis of nanocomposite cylinders reinforced by single-walled carbon nanotubes subjected to an impact load.

In this paper, for the dynamic stability analysis of carbon nanotube-reinforced functionally graded (CNTR-FG) cylindrical panels under static and periodic axial force, an energy formulation is first described. Then a system of Mathieu–Hill equations is obtained via the Ritz minimization procedure and parametric resonance responses are analyzed using Bolotin's [1] method. In the present *kp*-Ritz method, two-dimensional displacement fields are approximated by a set of mesh-free kernel particle functions and the boundary conditions are enforced by penalty method. The CNTs are assumed to be uniaxially aligned in axial direction and functionally graded in thickness direction of the panels and effective material properties of CNTR-FG cylindrical panels are estimated through a micromechanical model based on the Eshelby–Mori–Tanaka approach. Several computational simulation examples are presented to figure out the effects of volume fraction of carbon nanotubes, edge-to-radius ratio and radius-to-thickness ratio, boundary conditions and distribution types of CNTs.

2. Carbon nanotube-reinforced functionally graded cylindrical panels

The cylindrical panel considered in this paper (Fig. 1) has a coordinate system (x, θ, z) fixed on its middle surface. This panel is assumed to be thin and of length L, radius R, span angle θ_0 and thickness h. The CNTs are assumed to be uniaxially aligned in axial direction and functionally graded in thickness direction of the cylindrical panels with four different distributions denoted by UD, FG-V, FG-O and FG-X. According to distributions of CNTs (Fig. 2), CNT volume fractions $V_{\mathrm{CNT}}(z)$ are given by

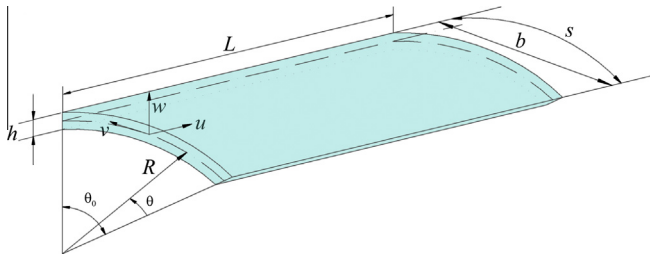

Fig. 1. Coordinate system and geometry properties of CNTR-FG cylindrical panel.

$$V_{\mathrm{CNT}}(z)=\begin{cases} V^*_{\mathrm{CNT}} & (\mathrm{UD}),\\ \left(1+\frac{2z}{h}\right)V^*_{\mathrm{CNT}} & (\mathrm{FG\text{-}V}),\\ 2\left(1-\frac{2|z|}{h}\right)V^*_{\mathrm{CNT}} & (\mathrm{FG\text{-}O}),\\ 2\left(\frac{2|z|}{h}\right)V^*_{\mathrm{CNT}} & (\mathrm{FG\text{-}X}), \end{cases} \tag{1}$$

where

$$V^*_{\mathrm{CNT}}=\frac{w_{\mathrm{CNT}}}{w_{\mathrm{CNT}}+(\rho^{\mathrm{CNT}}/\rho^m)-(\rho^{\mathrm{CNT}}/\rho^m)w_{\mathrm{CNT}}}, \tag{2}$$

where w_{CNT} is the fraction of mass of the CNTs and ρ^m and ρ^{CNT} are densities of the matrix and CNTs, respectively.

It has bee well described that the structure of CNTs can significantly affect the effective material properties of CNT-reinforced materials [23–26]; several micromechanical models have been proposed to estimate the effective material properties of the resulting nanocomposites, such as Eshelby–Mori–Tanaka scheme [27–29] and the extended rule of mixture [15,30,31]. According to Benveniste's revision [32], effective elastic module tensor $\mathbf{L}$ is expressed as

$$\mathbf{L}=\mathbf{L}_m+V_{\mathrm{CNT}}\langle(\mathbf{L}_{\mathrm{CNT}}-\mathbf{L}_m)\cdot\mathbf{A}\rangle\cdot[V_m\mathbf{I}+V_{\mathrm{CNT}}\langle\mathbf{A}\rangle]^{-1}, \tag{3}$$

where angle brackets represent an average over all possible orientation of the inclusions and $\mathbf{L}_m$ and $\mathbf{L}_{\mathrm{CNT}}$ are stiffness tensors of the matrix and the CNT, respectively. $\mathbf{I}$ is the fourth-order unit tensor and $\mathbf{A}$ is the diluted mechanical strain concentration tensor and is expressed as

$$\mathbf{A}=\left[\mathbf{I}+\mathbf{S}\cdot\mathbf{L}_m^{-1}\cdot(\mathbf{L}_{\mathrm{CNT}}-\mathbf{L}_m)\right]^{-1}, \tag{4}$$

where $\mathbf{S}$ is the fourth-order Eshelby tensor [33] and is well defined for cylindrical inclusions in [34].

3. Theoretical formulations

3.1. Energy formulation

The cylindrical panel described in Fig. 1 is bounded along its edges by the lines $x=0$, $x=L$, $\theta=0$ and $\theta=\theta_0$. The displacement components in x, y and z directions are represented by u, v and w, respectively. The extensional pulsating axial load is expressed as

$$N_a=N_0+N_s\cos Pt, \tag{5}$$

where P is the radian frequency of excitation per unit time.

The kinetic energy for the cylindrical panel is given by

$$\Theta=\frac{1}{2}\rho h\int_0^L\int_0^{\theta_0}(\dot{u}^2+\dot{v}^2+\dot{w}^2)R\,\mathrm{d}\theta\,\mathrm{d}x, \tag{6}$$

where $\dot{u}$, $\dot{v}$ and $\dot{w}$ are the linear velocities in x, θ and z directions, respectively.

The strain energy U_a due to the axial loading can be expressed as

$$U_a=\frac{1}{2}\int_0^L\int_0^{\theta_0}N_a\left[\left(\frac{\partial u}{\partial x}\right)^2+\left(\frac{\partial v}{\partial x}\right)^2+\left(\frac{\partial w}{\partial x}\right)^2\right]R\,\mathrm{d}\theta\,\mathrm{d}x. \tag{7}$$

The strain energy of the cylindrical panel can be written as

$$U_\varepsilon=\frac{1}{2}\int_0^L\int_0^{\theta_0}\boldsymbol{\varepsilon}^T\mathbf{S}\boldsymbol{\varepsilon}R\,\mathrm{d}\theta\,\mathrm{d}x, \tag{8}$$

where

$$\boldsymbol{\varepsilon}=(e_1\quad e_2\quad\gamma\quad\kappa_1\quad\kappa_2\quad 2\tau), \tag{9}$$

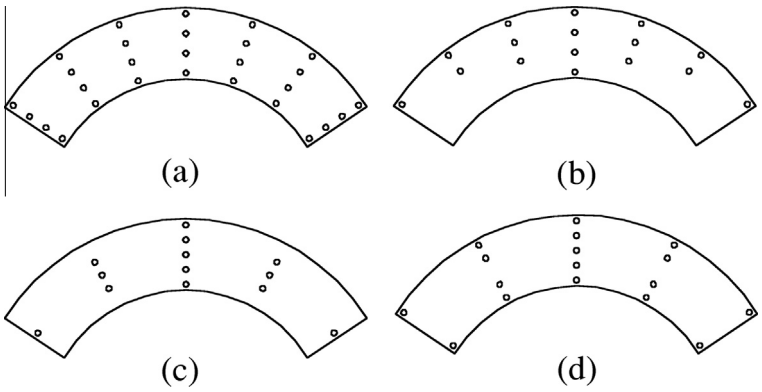

Fig. 2. Distribution types of CNTs of CNTR-FG cylindrical panels in the thickness direction. (a) UD panel; (b) FG-V panel; (c) FG-O panel; and (d) FG-X panel.

$$\mathbf{S}=\begin{bmatrix} A_{11} & A_{12} & A_{16} & B_{11} & B_{12} & B_{12} \\ A_{12} & A_{22} & A_{26} & B_{12} & B_{22} & B_{26} \\ A_{16} & A_{26} & A_{66} & B_{16} & B_{26} & B_{66} \\ B_{11} & B_{12} & B_{16} & D_{11} & D_{12} & D_{16} \\ B_{12} & B_{22} & B_{26} & D_{12} & D_{22} & D_{26} \\ B_{16} & B_{26} & B_{66} & D_{16} & D_{26} & D_{66} \end{bmatrix}=\begin{bmatrix} \mathbf{A} & \overline{\mathbf{B}} \\ \overline{\mathbf{B}} & \mathbf{D} \end{bmatrix}, \tag{10}$$

in which the extensional A_{ij}, coupling B_{ij} and bending D_{ij} stiffness are given by

$$(A_{ij}, B_{ij}, D_{ij})=\int_{-h/2}^{h/2} Q_{ij}(1, z, z^2)\mathrm{d}z, \tag{11}$$

where Q_{ij} are the engineering constants related to material properties, which can be written as

$$Q_{11}=\frac{E_{11}}{1-\nu_{12}\nu_{21}}, \quad Q_{22}=\frac{E_{22}}{1-\nu_{12}\nu_{21}}, \quad Q_{12}=\frac{\nu_{21}E_{11}}{1-\nu_{12}\nu_{21}}, \tag{12}$$

$$Q_{66}=G_{12}, \tag{13}$$

and the middle surface strains e_1, e_2 and γ and the middle surface curvatures κ_1, κ_2 and τ are defined according to Love's thin shell theory

$$e_1=\frac{\partial u}{\partial x}, \quad e_2=\frac{1}{R}\left(\frac{\partial v}{\partial \theta}+w\right), \tag{14}$$

$$\gamma=\frac{\partial v}{\partial x}+\frac{1}{R}\frac{\partial v}{\partial \theta}, \quad \kappa_1=-\frac{\partial^2 w}{\partial^2 x}, \tag{15}$$

$$\kappa_2=-\frac{1}{R^2}\left(\frac{\partial^2 w}{\partial^2 \theta}-\frac{\partial v}{\partial \theta}\right), \quad \tau=-\frac{1}{R}\left(\frac{\partial^2 w}{\partial x \partial \theta}-\frac{\partial v}{\partial x}\right). \tag{16}$$

Therefore, the total energy functional of the panel is obtained as

$$\Pi_f=\Theta-U_\varepsilon-U_a. \tag{17}$$

3.2. Discrete system equations

For a cylindrical panel domain discretized by a set of nodes $\boldsymbol{x}_I$, $I=1,\ldots,NP$, the discrete displacement approximations are expressed as

$$(u, v, w)^T=\sum_{I=1}^{NP}\psi_I(\boldsymbol{x})(u_I, v_I, w_I)^T e^{i\omega t}=\sum_{I=1}^{NP}\psi_I(\boldsymbol{x})\mathbf{u}_I e^{i\omega t}, \tag{18}$$

where $\boldsymbol{u}_I$ is the nodal parameter and $\psi_I(\boldsymbol{x})$ is the shape function of displacements u, v and w, defined as [35,36]:

$$\psi_I(\boldsymbol{x})=C(\boldsymbol{x};\boldsymbol{x}-\boldsymbol{x}_I)\Phi_a(\boldsymbol{x}-\boldsymbol{x}_I), \tag{19}$$

where $\Phi_a(\boldsymbol{x}-\boldsymbol{x}_I)$ is the kernel function. $C(\boldsymbol{x};\boldsymbol{x}-\boldsymbol{x}_I)$ is the correction function, defined as:

$$C(\boldsymbol{x};\boldsymbol{x}-\boldsymbol{x}_I)=\mathbf{H}^T(\boldsymbol{x}-\boldsymbol{x}_I)\mathbf{b}(\boldsymbol{x}), \tag{20}$$

$$\mathbf{b}(\boldsymbol{x})=[b_0(x,\theta), b_1(x,\theta), b_2(x,\theta), b_3(x,\theta), b_4(x,\theta), b_5(x,\theta)]^{\mathrm{T}}, \tag{21}$$

$$\mathbf{H}^{\mathrm{T}}(\boldsymbol{x}-\boldsymbol{x}_I)=[1, x-x_I, \theta-\theta_I, (x-x_I)(\theta-\theta_I), (x-x_I)^2, (\theta-\theta_I)^2]. \tag{22}$$

The shape function thus is:

$$\psi_I(\boldsymbol{x})=\mathbf{b}^{\mathrm{T}}(\boldsymbol{x})\mathbf{H}(\boldsymbol{x}-\boldsymbol{x}_I)\Phi_a(\boldsymbol{x}-\boldsymbol{x}_I), \tag{23}$$

and Eq. (23) can be rewritten as:

$$\psi_I(\boldsymbol{x})=\mathbf{b}^{\mathrm{T}}(\boldsymbol{x})\mathbf{B}_I(\boldsymbol{x}-\boldsymbol{x}_I), \tag{24}$$

where

$$\mathbf{b}(\boldsymbol{x})=\mathbf{M}^{-1}(\boldsymbol{x})\mathbf{H}(0), \tag{25}$$

$$\mathbf{B}_I(\boldsymbol{x}-\boldsymbol{x}_I)=\mathbf{H}(\boldsymbol{x}-\boldsymbol{x}_I)\Phi_a(\boldsymbol{x}-\boldsymbol{x}_I), \tag{26}$$

in which

$$\mathbf{M}(\boldsymbol{x})=\sum_{I=1}^{NP}\mathbf{H}(\boldsymbol{x}-\boldsymbol{x}_I)\mathbf{H}^{\mathrm{T}}(\boldsymbol{x}-\boldsymbol{x}_I)\Phi_a(\boldsymbol{x}-\boldsymbol{x}_I), \tag{27}$$

$$\mathbf{H}(\mathbf{0})=[1,0,0,0,0,0,]^{\mathrm{T}}. \tag{28}$$

For the two-dimensional problem, the kernel function $\Phi_a(\boldsymbol{x}-\boldsymbol{x}_I)$ can be written as

$$\Phi_a(\boldsymbol{x}-\boldsymbol{x}_I)=\Phi_a(\boldsymbol{x})\cdot\Phi_a(\theta), \tag{29}$$

where

$$\Phi_a(x)=\varphi\left(\frac{x-x_I}{a}\right). \tag{30}$$

In the present study, the cubic spline function is selected as the weight function, given by

$$\varphi_z(z_I)=\begin{Bmatrix} \frac{2}{3}-4z_I^2+4z_I^3 & \text{for } 0\leqslant|z_I|\leqslant\frac{1}{2} \\ \frac{4}{3}-4z_I+4z_I^2-\frac{4}{3}z_I^3 & \text{for } \frac{1}{2}<|z_I|\leqslant 1 \\ 0 & \text{otherwise} \end{Bmatrix}, \tag{31}$$

where $z_I=\frac{x-x_I}{d_I}$ and d_I is the size of the support of node I, calculated by

$$d_I=d_{\max}c_I, \tag{32}$$

where distance c_I is chosen by searching for a sufficient number of nodes to avoid the singularity of matrix $\mathbf{M}$ and $d_{\max}$ is a scaling factor ranging from 2.0 to 4.0.

Therefore, the shape function can be expressed as

$$\psi_I(\boldsymbol{x})=\mathbf{H}^{\mathrm{T}}(\mathbf{0})\mathbf{M}^{-1}(\boldsymbol{x})\mathbf{H}(\boldsymbol{x}-\boldsymbol{x}_I)\Phi_a(\boldsymbol{x}-\boldsymbol{x}_I). \tag{33}$$

Eq. (25) can be rewritten as

$$\mathbf{M}(\boldsymbol{x})\mathbf{b}(\boldsymbol{x})=\mathbf{H}(0). \tag{34}$$

Followed by the back substitution, the vector $\mathbf{b}(\boldsymbol{x})$ can be determined by using the LU decomposition of the matrix $\mathbf{M}(\boldsymbol{x})$. Taking the first derivative of Eq. (34), we can obtain

$$\mathbf{M}_{,x}(\boldsymbol{x})\mathbf{b}(\boldsymbol{x}) + \mathbf{M}(\boldsymbol{x})\mathbf{b}_{,x}(\boldsymbol{x}) = \mathbf{H}_{,x}(0), \tag{35}$$

which can be rearranged as

$$\mathbf{M}(\boldsymbol{x})\mathbf{b}_{,x}(\boldsymbol{x}) = \mathbf{H}_{,x}(0) - \mathbf{M}_{,x}(\boldsymbol{x})\mathbf{b}(\boldsymbol{x}). \tag{36}$$

It is noted that the first derivative of $\mathbf{b}(\boldsymbol{x})$ can be derived again using the LU decomposition procedure.

Now, the first derivative of the shape function can be obtained by taking the derivative of Eq. (33), i.e.

$$\psi_{I,x}(\boldsymbol{x}) = \mathbf{b}_{,x}^{\mathrm{T}}(\boldsymbol{x})\mathbf{B}_I(\boldsymbol{x}-\boldsymbol{x}_I) + \mathbf{b}^{\mathrm{T}}(\boldsymbol{x})\mathbf{B}_{I,x}(\boldsymbol{x}-\boldsymbol{x}_I). \tag{37}$$

It is worth noting that the second derivative of the shape function can also be obtained by using the same procedure.

Since the shape function $\psi_I(\boldsymbol{x})$ in the present mesh-free method does not possess Kronecker delta property, the essential boundary conditions cannot be directly imposed. Several approaches have been proposed to enforce essential boundary conditions for mesh-free methods, such as the transformation method, Lagrange multipliers approach, the penalty method, and modified variational principles. In this study, the penalty method [37,38] is employed to implement essential boundary conditions.

Simply supported boundary conditions:

For the domain bounded by l_u, the displacement boundary condition is

$$\mathbf{u} = \bar{\mathbf{u}}, \tag{38}$$

where $\bar{\mathbf{u}}$ is the prescribed displacement on the displacement boundary l_u. The variational form is expressed as

$$\Gamma_{\bar{u}} = \frac{\bar{\alpha}}{2}\int_{l_u}(\mathbf{u}-\bar{\mathbf{u}})^T(\mathbf{u}-\bar{\mathbf{u}})\mathrm{d}l, \tag{39}$$

where $\bar{\alpha}$ is the penalty parameter which is taken as 10^3E_{11}.

Clamped boundary conditions:

For the clamped boundary condition, in addition to the boundary condition described by Eq. (34), the rotation boundary condition is also included

$$\boldsymbol{\beta} = \bar{\boldsymbol{\beta}}, \tag{40}$$

where

$$\boldsymbol{\beta} = \frac{\mathrm{d}w}{\mathrm{d}\boldsymbol{x}}, \tag{41}$$

and $\bar{\boldsymbol{\beta}}$ is the prescribed rotation on the boundary. The variational form due to the rotation can also be written as

$$\Gamma_{\bar{\beta}} = \frac{\bar{\alpha}}{2}\int_{l_u}(\boldsymbol{\beta}-\bar{\boldsymbol{\beta}})^T(\boldsymbol{\beta}-\bar{\boldsymbol{\beta}})\mathrm{d}l. \tag{42}$$

Thus, the variational form due to the boundary conditions can be given by

$$\Gamma_B = \Gamma_{\bar{u}} + \Gamma_{\bar{\beta}}. \tag{43}$$

Eventually, the total energy functional for the present problem becomes

$$\Gamma = \Gamma_t + \Gamma_B. \tag{44}$$

Substituting Eq. (18) into the total energy functional applying the Rayleigh–Ritz minimization procedure, we can obtain a system of Mathieu–Hill equations as

$$\widetilde{\mathbf{M}}\ddot{\mathbf{q}} + (\widetilde{\mathbf{K}} - \cos Pt\mathbf{Q})\mathbf{q} = 0, \tag{45}$$

where

$$\widetilde{\mathbf{K}} = \boldsymbol{\Lambda}^{-1}\mathbf{K}\boldsymbol{\Lambda}^{-\mathrm{T}}, \quad \widetilde{\mathbf{M}} = \boldsymbol{\Lambda}^{-1}\overline{\mathbf{M}}\boldsymbol{\Lambda}^{-\mathrm{T}}. \tag{46}$$

Matrices $\boldsymbol{\Lambda}$, $\mathbf{K}$ and $\mathbf{M}$ are given as follows:

$$\boldsymbol{\Lambda}_{IJ} = \psi_I(x_J)\boldsymbol{I}, \quad \boldsymbol{I} \text{ is the identity matrix}, \tag{47}$$

$$\mathbf{K} = \mathbf{K}^{\varepsilon} + \mathbf{K}^{A} + \mathbf{K}^{B_1} + \mathbf{K}^{B_2}, \tag{48}$$

$$\mathbf{K}_{IJ}^{\varepsilon} = \int_0^L\int_0^{\theta_0}(\mathbf{B}_I^{\varepsilon})^{\mathrm{T}}\mathbf{S}\mathbf{B}_J^{\varepsilon}R\,\mathrm{d}\theta\,\mathrm{d}x, \tag{49}$$

$$\mathbf{K}_{IJ}^{A} = \int_0^L\int_0^{\theta_0}\left(\mathbf{B}_I^{A}\right)^{\mathrm{T}}N_0\mathbf{B}_J^{A}R\,\mathrm{d}\theta\,\mathrm{d}x, \tag{50}$$

$$\mathbf{K}_{IJ}^{B_1} = \bar{\alpha}\int_u\left(\mathbf{B}1_I^{B}\right)^{\mathrm{T}}\mathbf{B}1_J^{B}\,\mathrm{d}l, \tag{51}$$

$$\mathbf{K}_{IJ}^{B_2} = \bar{\alpha}\int_u\left(\mathbf{B}2_I^{B}\right)^{\mathrm{T}}\mathbf{B}2_J^{B}\,\mathrm{d}l, \tag{52}$$

$$\overline{\mathbf{M}} = \rho h\int_0^L\int_0^{\theta_0}\mathbf{M}_I^{\mathrm{T}}\mathbf{M}_J R\,\mathrm{d}\theta\,\mathrm{d}x, \tag{53}$$

where

$$\mathbf{B}_I^{b} = \begin{bmatrix} \frac{\partial\psi_I}{\partial x} & 0 & 0 \\ 0 & \frac{1}{R}\frac{\partial\psi_I}{\partial x} & \frac{\psi_I}{R} \\ \frac{1}{R}\frac{\partial\psi_I}{\partial\theta} & \frac{\partial\psi_I}{\partial x} & 0 \\ 0 & 0 & -\frac{\partial^2\psi_I}{\partial x^2} \\ 0 & \frac{1}{R^2}\frac{\partial\psi_I}{\partial\theta} & -\frac{1}{R^2}\frac{\partial^2\psi_I}{\partial\theta^2} \\ 0 & \frac{2}{R}\frac{\partial\psi_I}{\partial x} & -\frac{2}{R}\frac{\partial^2\psi_I}{\partial x\partial\theta} \end{bmatrix}, \tag{54}$$

$$\mathbf{B}1_I^{B} = \begin{bmatrix} \psi_I & 0 & 0 \\ 0 & \psi_I & 0 \\ 0 & 0 & \psi_I \end{bmatrix}, \tag{55}$$

$$\mathbf{B}2_I^{B} = \begin{bmatrix} \frac{\partial\psi_I}{\partial x} & 0 & 0 \\ 0 & \frac{\partial\psi_I}{\partial x} & 0 \\ 0 & 0 & \frac{\partial\psi_I}{\partial x} \end{bmatrix}, \tag{56}$$

$$\mathbf{M}_I = \begin{bmatrix} \psi_I & 0 & 0 \\ 0 & \psi_I & 0 \\ 0 & 0 & \psi_I \end{bmatrix}. \tag{57}$$

The governing equation (Eq. (45)) is a second order differential equation with periodic coefficients of the Mathieu–Hill type. The instability regions are separated by the periodic solutions with periods T and $2T$ ($T = 2\pi/P$). Since the widths of the solutions with period $2T$ are usually larger than those associated with solutions having period of T, the solutions with period $2T$ are of greater practical importance. By using Bolotin's approach as a first approximation, the periodic solutions with period $2T$ can be sought in the form

$$\bar{\mathbf{q}} = \bar{\mathbf{f}}\sin\frac{Pt}{2} + \bar{\mathbf{g}}\cos\frac{Pt}{2}, \tag{58}$$

where $\bar{\mathbf{f}}$ and $\bar{\mathbf{g}}$ are arbitrary vectors.

Substituting Eq. (58) into Eq. (45) and equating the coefficients of $\sin Pt = 2$ and $\cos Pt = 2$ terms, we can obtain a set of linear homogeneous algebraic equations in terms of $\bar{\mathbf{f}}$ and $\bar{\mathbf{g}}$. The conditions of non-trivial solutions are expressed as

$$\det\left[\begin{pmatrix} -\frac{1}{4}P^2\widetilde{\mathbf{M}}_{IJ} + \widetilde{\mathbf{K}} - \frac{1}{2}\mathbf{Q}_{IJ} & 0 \\ 0 & -\frac{1}{4}P^2\widetilde{\mathbf{M}}_{IJ} + \widetilde{\mathbf{K}} + \frac{1}{2}\mathbf{Q}_{IJ} \end{pmatrix}\right] = 0. \tag{59}$$

Since it is more complicated to solve the above nonlinear geometric equations for P, the above expression is rearranged to the standard form of a generalized eigenvalue problem

$$\det\left[\begin{pmatrix} \widetilde{\mathbf{K}} - \frac{1}{2}\mathbf{Q}_{IJ} & 0 \\ 0 & \widetilde{\mathbf{K}} + \frac{1}{2}\mathbf{Q}_{IJ} \end{pmatrix} - P^2\begin{pmatrix} \frac{1}{4}\widetilde{\mathbf{M}}_{IJ} & 0 \\ 0 & \frac{1}{4}\widetilde{\mathbf{M}}_{IJ} \end{pmatrix}\right] = 0. \tag{60}$$

The boundaries between the stable and unstable regions can be defined by the generalized eigenvalues P^2 of the above generalized eigenvalue problem.

4. Numerical results

For CNTR-FG cylindrical panels considered in this paper, Poly (methyl methacrylate), referred as PMMA, is selected as the matrix with material properties $\upsilon_m = 0.34$, $\alpha^m = 45(1 + 0.0005\Delta T) \times 10^{-6}/\mathrm{K}$ and $E^m = (3.52 - 0.0034T)$ GPa, where $T = T_0 + \Delta T$ and $T_0 = 300$ K (room temperature). (10,10) SWCNTs are selected as reinforcement. Han and Elliott [39] have reported that modulus of (10,10) SWCNTs ($E_{11}^{CNT} = 600$ GPa, $E_{22}^{CNT} = 10$ GPa, $G_{12}^{CNT} = 17.2$ GPa). The main cause of such a low value is that the effective thickness of CNTs is assumed as 0.34 nm. However it is reported that the effective thickness of SWCNTs should be smaller than 0.142 nm and, therefore, material properties of SWCNTs used for the present study are selected from MD simulation results reported by Shen and Zhang [40] where effective wall thickness obtained for (10,10) SWCNTs is 0.067 nm, which satisfies the Vodenitcharova-Zhang criterion [41].

4.1. Isotropic cylindrical panel

To validate the present formulation, analysis of an isotropic cylindrical panel under tensile and compressive loads is carried out to assess the accuracy of the present methodology. The isotropic cylindrical panel has parameters of $b/R = 0.5$, $L/R = 2$ and $\upsilon = 0.3$. It is obvious that the compressive or tensile periodic axial load cannot exceed the critical buckling load of the cylindrical shell panel. In the present study, the buckling load for isotropic cylindrical shell panel of intermediate length is given as [42]

$$N_{buc} = \frac{Eh^2}{[3(1-\nu^2)]^{1/2}R}, \tag{61}$$

where E and υ are the elastic modulus and Poisson's ratio of the isotropic cylindrical panel, respectively. The non-dimensional frequency parameter $\overline{P}$ is defined as

$$\overline{P} = RP\sqrt{\frac{\rho(1-\nu^2)}{E}}. \tag{62}$$

Each unstable region is bounded by two curves originating from a common point from the $\overline{P}$ axis with $N_s = 0$. The present numerical solutions are tabulated in Table 1 which are compared with results of Ng et al. [43] using classical shell theory (CST) and first order shear deformation theory (FSDT). The first four modes of isotropic cylindrical panel are ($m = 1$, $n = 1$), ($m = 2$, $n = 1$), ($m = 3$, $n = 1$) and ($m = 4$, $n = 1$). It can be seen that the present results agree well with those given by Ng et al. [43].

4.2. CNTR-FG cylindrical panels

The instability regions of CNTR-FG cylindrical panels having different boundary conditions are investigated in this section. The span angle of the panel is chosen to be $\theta_0 = 60°$. The edge-to-radius ratio, L/R, varies from 1.0 to 3.0. The CNT volume fraction (V_{CNT}) changes from 0.11 to 0.17, and the radius-to-thickness ratio (R/H) is selected as 200–300. For CNTR-FG cylindrical panels, the critical buckling load N_{cr} is approximated as

$$N_{cr} = \frac{E_{22}h^2}{[3(1-\nu_{12}\nu_{21})]^{1/2}R}, \tag{63}$$

and the non-dimensional frequency parameter $\overline{P}$ is defined as

$$\overline{P} = RP\sqrt{\frac{\rho(1-\nu_{12}\nu_{21})}{E_{22}}}. \tag{64}$$

The static axial force is selected as $N_0 = 0.5N_{cr}$.

Fig. 3 shows the first four unstable regions of a UD CNTR-FG cylindrical panel having radius-to-thickness ratio $R/H = 200$ under simply supported boundary conditions. The CNT volume fraction V_{CNT} is assumed to be 0.11 and the edge-to-radius ratio is selected as $L/R = 1.0$. These first four modes correspond to ($m = 1$, $n = 1$), ($m = 1$, $n = 2$), ($m = 1$, $n = 3$) and ($m = 1$, $n = 4$). It is found that the first mode ($m = 1$, $n = 1$) has the largest instability region, followed in descending order by modes ($m = 1$, $n = 2$), ($m = 1$, $n = 3$) and ($m = 1$, $n = 4$); the last has the smallest instability region. The corresponding first four unstable regions for other three types CNTR-FG cylindrical panels FG-V, FG-O and FG-X are depicted in Figs. 4–6. Some similar phenomenon about the order of the region size is observed. In our earlier studies about CNTR-FG plate and panel [19,44–47], we found that CNTs distributed close to top and bottom surfaces are more efficient in increasing the stiffness of the plate or panel than CNTs distributed near the mid-surface. In the present dynamic stability analysis, it is also discovered that the non-dimensional frequency parameter for FG-X and FG-O type panels have the maximum and minimum value, and those of UD and FG-V panels lie between FG-X and FG-O. As the radius-to-thickness ratio (R/H) increases from 200 to 300, the first four unstable regions of these four types CNTR-FG cylindrical panels are shown in Figs. 7–10. It can be seen that the instability regions of modes 1 and 2 are overlapping as N_s/N_0 exceeds 0.35 for UD and FG-V type panels, 0.43 for FG-O type panel and 0.28 for FG-X panel.

Table 1
Comparisons of unstable regions for an isotropic cylindrical panel under tensile and compressive loads with simply supported boundary condition.

h/R	Mode	Point of origin					
		Compressive loading			Tensile loading		
		CST [43]	FSDT [43]	Present	CST [43]	FSDT [43]	Present
0.03	(1,1)	0.6533	0.6483	0.6411	0.7651	0.7606	0.7592
	(2,1)	0.7182	0.7111	0.7004	1.0722	1.0665	1.0699
	(3,1)	0.9172	0.9061	0.9081	1.5076	1.4988	1.4953
	(4,1)	1.1958	1.1776	1.1571	1.9976	1.9832	1.9974
0.04	(1,1)	0.8854	0.874	0.8821	0.9977	0.987	0.9765
	(2,1)	0.9716	0.955	0.9517	1.3375	1.3236	1.3241
	(3,1)	1.2024	1.1761	1.1607	1.8313	1.8103	1.8195
	(4,1)	1.5495	1.5064	1.5138	2.4111	2.3769	2.4163
0.05	(1,1)	1.1183	1.0964	1.0798	1.2308	1.2106	1.2108
	(2,1)	1.2347	1.203	1.2005	1.6063	1.5791	1.5877
	(3,1)	1.5135	1.4632	1.4757	2.1621	2.1209	2.1483
	(4,1)	1.9419	1.8595	1.8993	2.8345	2.7679	2.8317

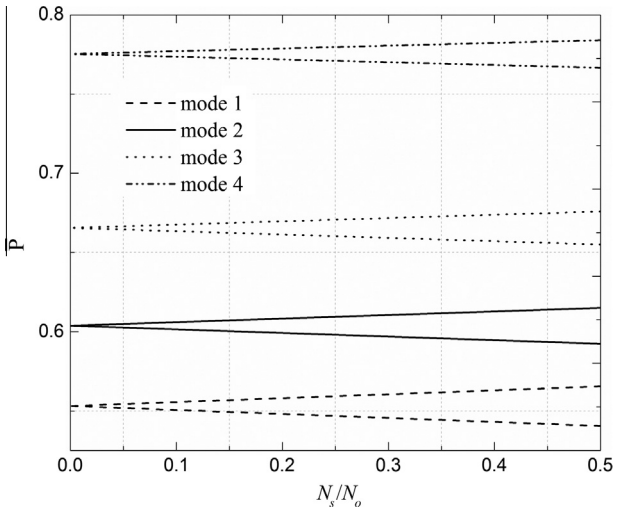

Fig. 3. Unstable regions for the first four modes of UD CNTR-FG cylindrical panel with $R/H = 200$ under SSSS boundary conditions.

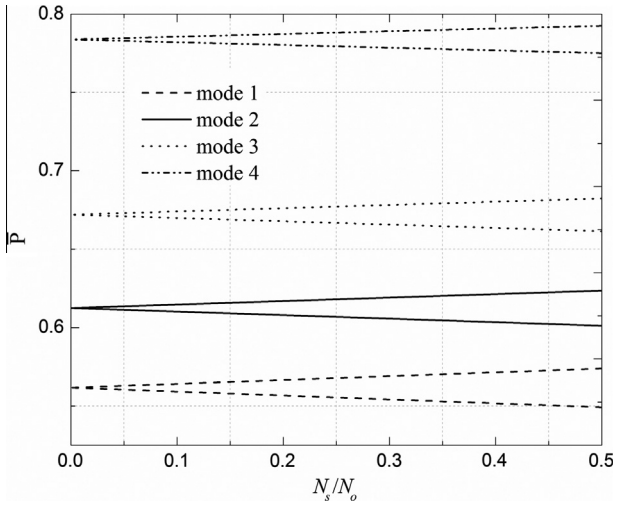

Fig. 4. Unstable regions for the first four modes of FG-V CNTR-FG cylindrical panel with $R/H = 200$ under SSSS boundary conditions.

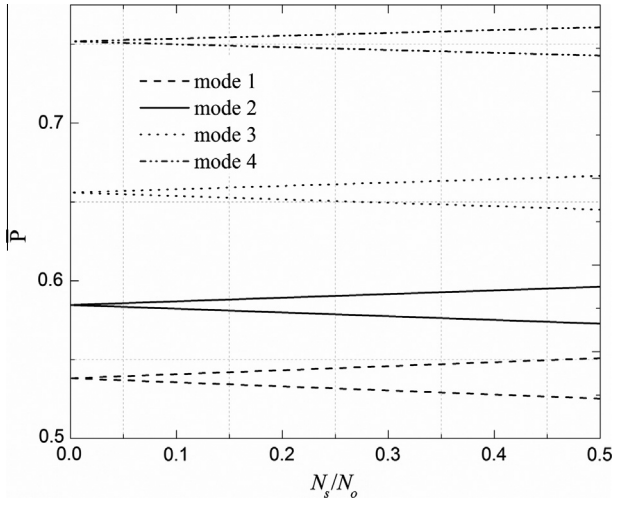

Fig. 5. Unstable regions for the first four modes of FG-O CNTR-FG cylindrical panel with $R/H = 200$ under SSSS boundary conditions.

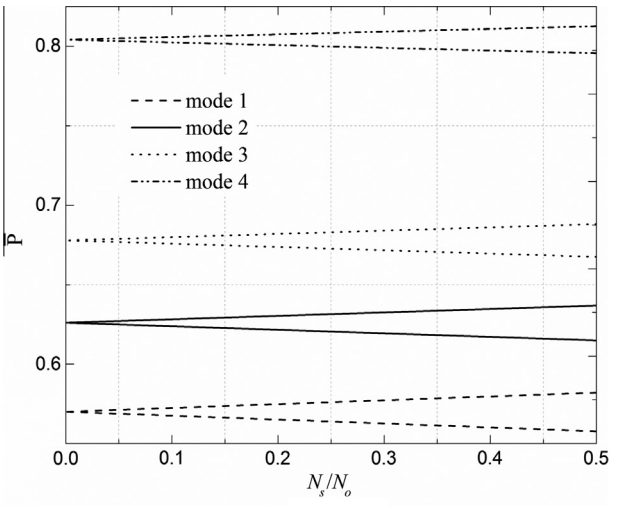

Fig. 6. Unstable regions for the first four modes of FG-X CNTR-FG cylindrical panel with $R/H = 200$ under SSSS boundary conditions.

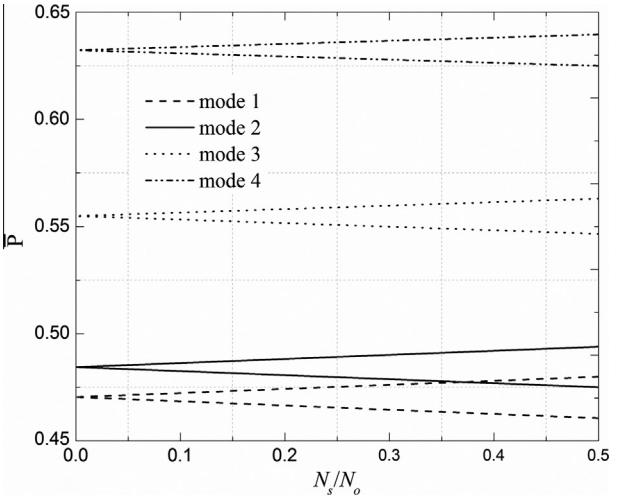

Fig. 7. Unstable regions for the first four modes of UD CNTR-FG cylindrical panel with $R/H = 300$ under SSSS boundary conditions.

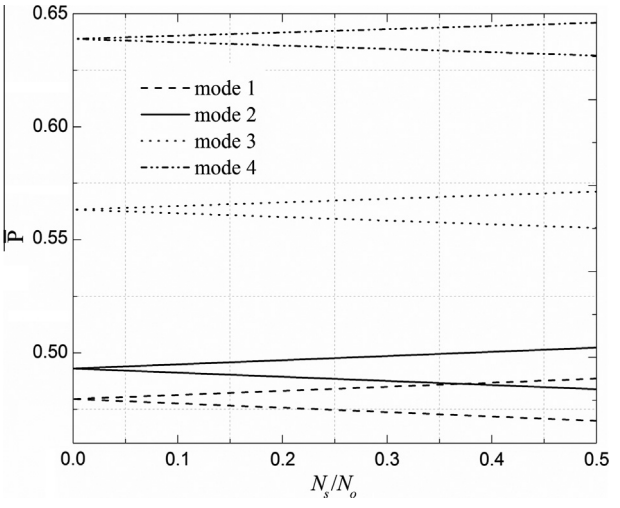

Fig. 8. Unstable regions for the first four modes of FG-V CNTR-FG cylindrical panel with $R/H = 300$ under SSSS boundary conditions.

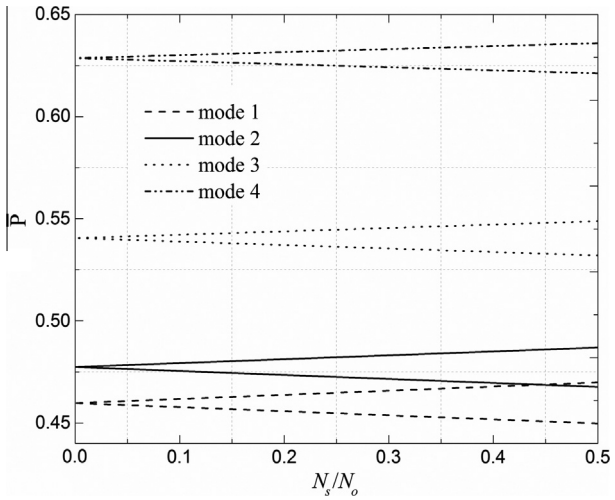

Fig. 9. Unstable regions for the first four modes of FG-O CNTR-FG cylindrical panel with $R/H = 300$ under SSSS boundary conditions.

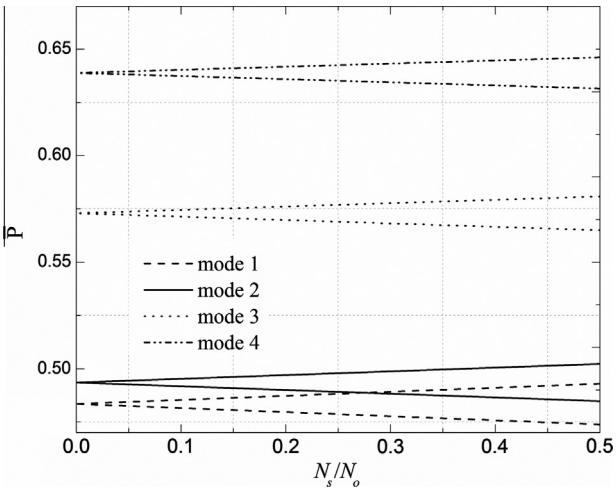

Fig. 10. Unstable regions for the first four modes of FG-X CNTR-FG cylindrical panel with $R/H = 300$ under SSSS boundary conditions.

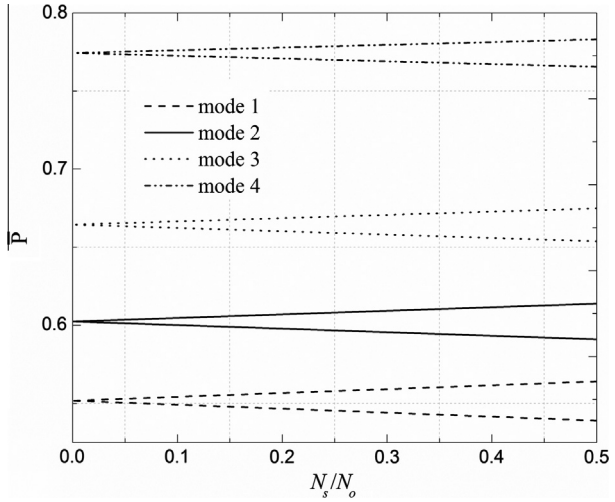

Fig. 11. Unstable regions for the first four modes of UD CNTR-FG cylindrical panel with $V_{CNT} = 0.14$ under SSSS boundary conditions.

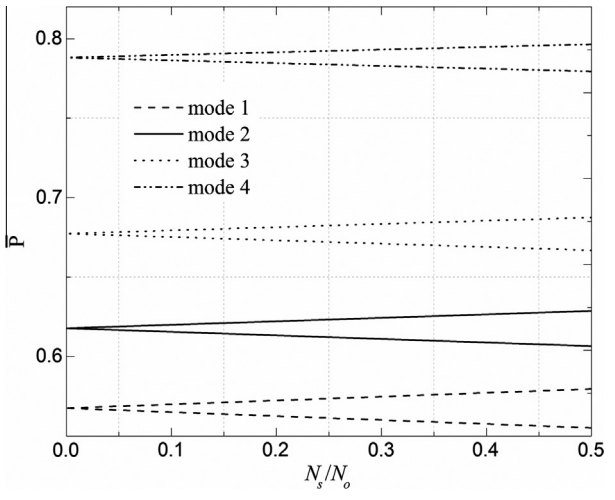

Fig. 12. Unstable regions for the first four modes of FG-V CNTR-FG cylindrical panel with $V_{CNT} = 0.14$ under SSSS boundary conditions.

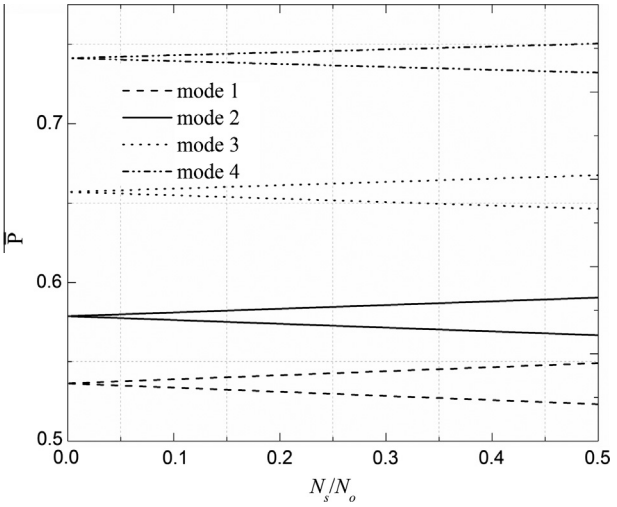

Fig. 13. Unstable regions for the first four modes of FG-O CNTR-FG cylindrical panel with $V_{CNT} = 0.14$ under SSSS boundary conditions.

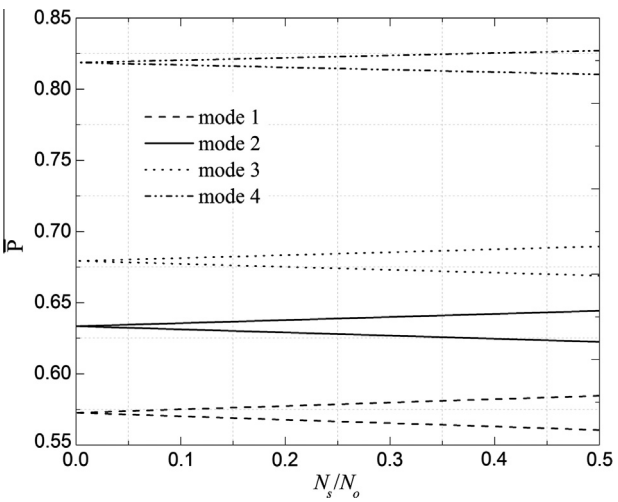

Fig. 14. Unstable regions for the first four modes of FG-X CNTR-FG cylindrical panel with $V_{CNT} = 0.14$ under SSSS boundary conditions.

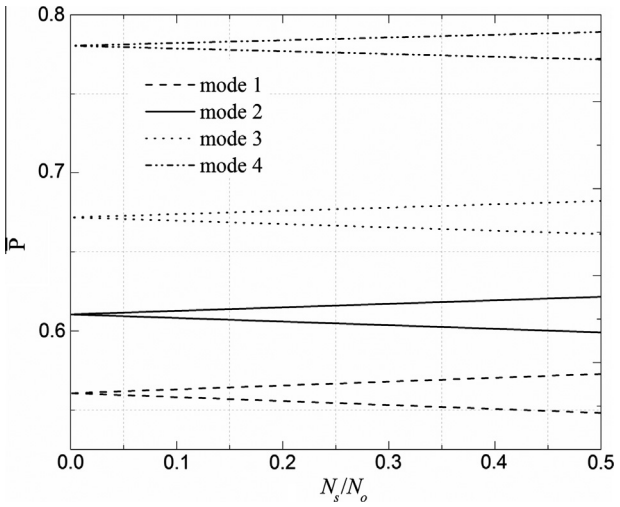

Fig. 15. Unstable regions for the first four modes of UD CNTR-FG cylindrical panel with $V_{CNT} = 0.17$ under SSSS boundary conditions.

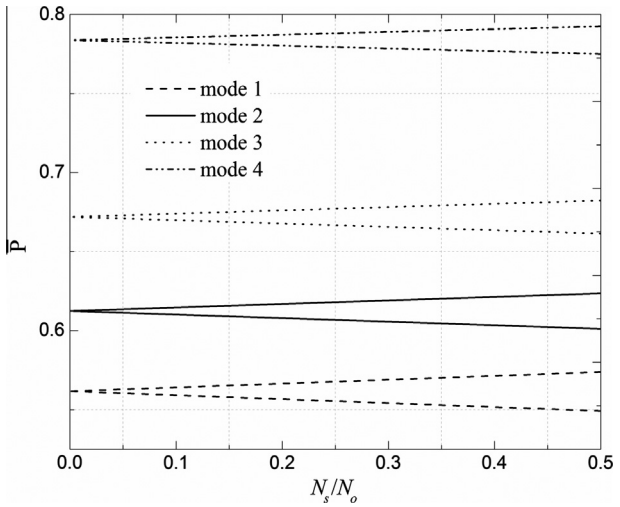

Fig. 16. Unstable regions for the first four modes of FG-V CNTR-FG cylindrical panel with $V_{CNT} = 0.17$ under SSSS boundary conditions.

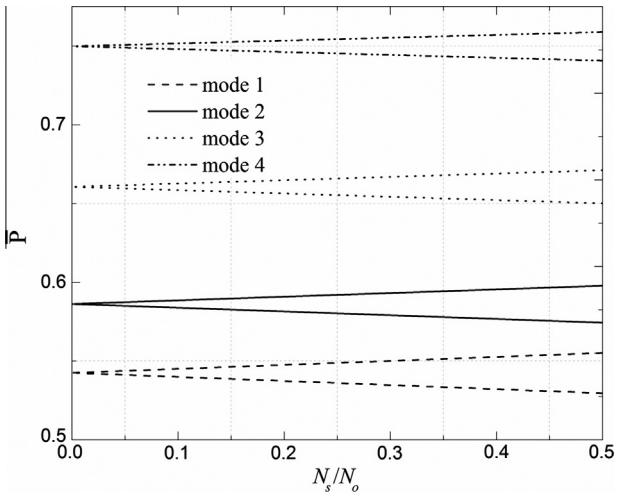

Fig. 17. Unstable regions for the first four modes of FG-O CNTR-FG cylindrical panel with $V_{CNT} = 0.17$ under SSSS boundary conditions.

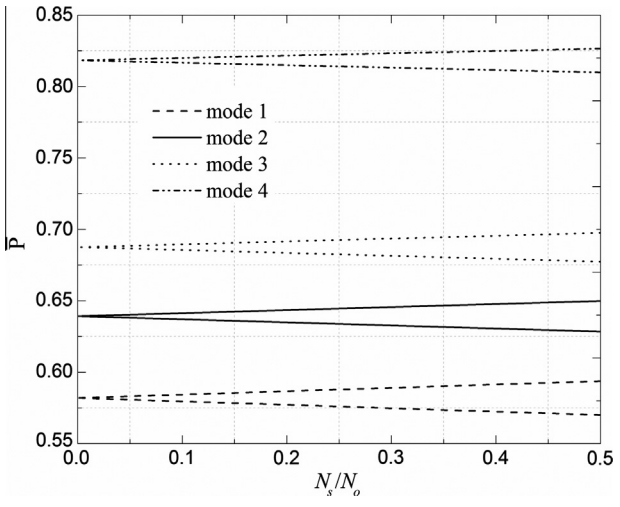

Fig. 18. Unstable regions for the first four modes of FG-X CNTR-FG cylindrical panel with $V_{CNT} = 0.17$ under SSSS boundary conditions.

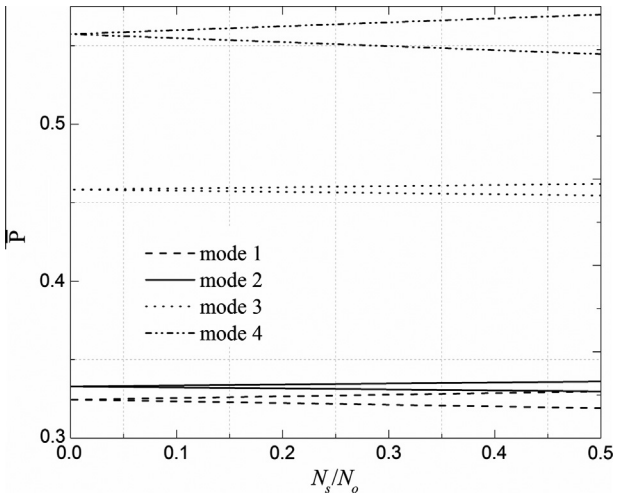

Fig. 19. Unstable regions for the first four modes of UD CNTR-FG cylindrical panel with $L/R = 2.0$ under SSSS boundary conditions.

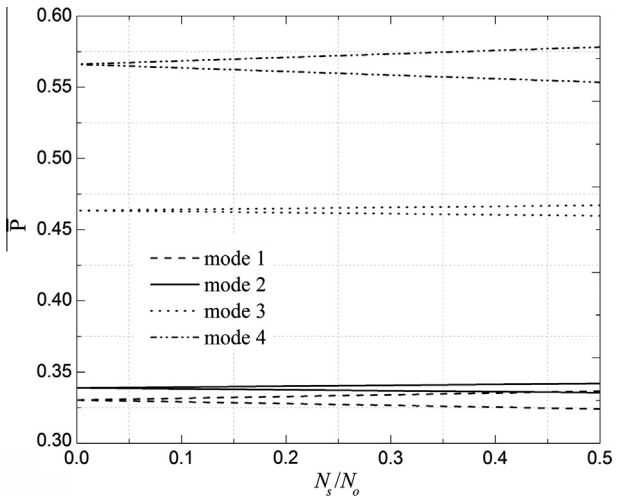

Fig. 20. Unstable regions for the first four modes of FG-V CNTR-FG cylindrical panel with $L/R = 2.0$ under SSSS boundary conditions.

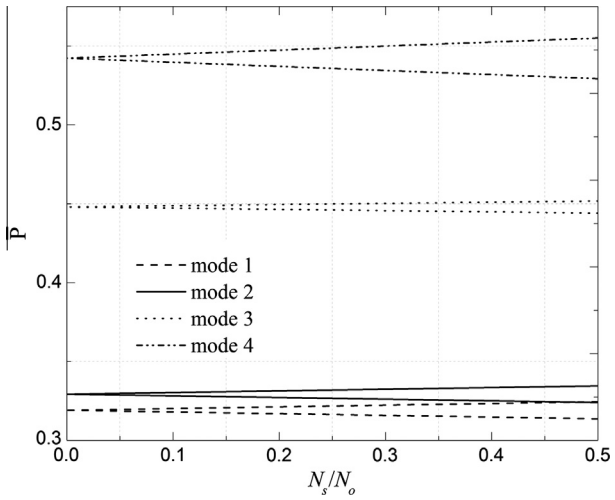

Fig. 21. Unstable regions for the first four modes of FG-O CNTR-FG cylindrical panel with $L/R = 2.0$ under SSSS boundary conditions.

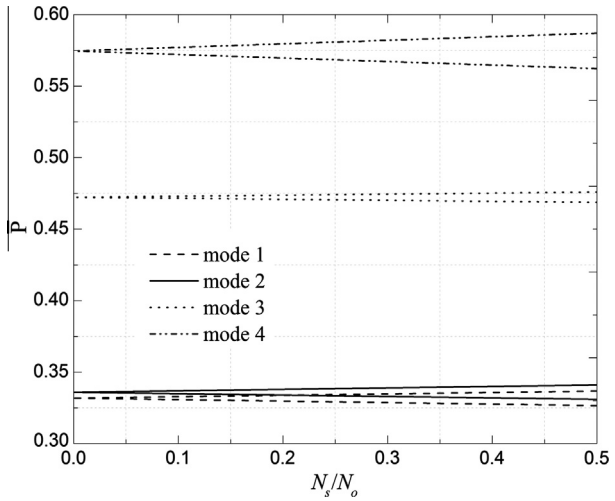

Fig. 22. Unstable regions for the first four modes of FG-X CNTR-FG cylindrical panel with $L/R = 2.0$ under SSSS boundary conditions.

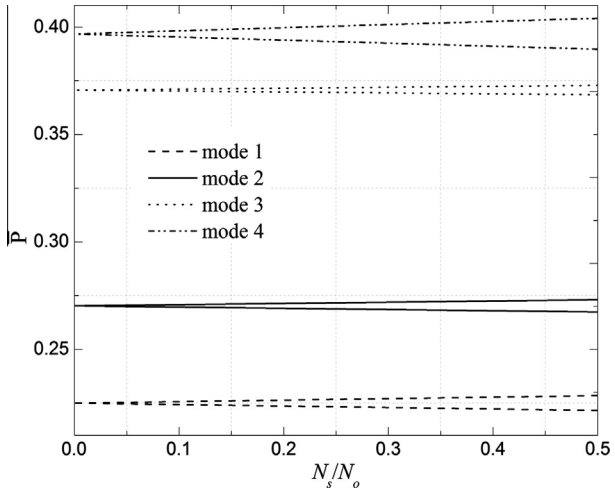

Fig. 23. Unstable regions for the first four modes of UD CNTR-FG cylindrical panel with $L/R = 3.0$ under SSSS boundary conditions.

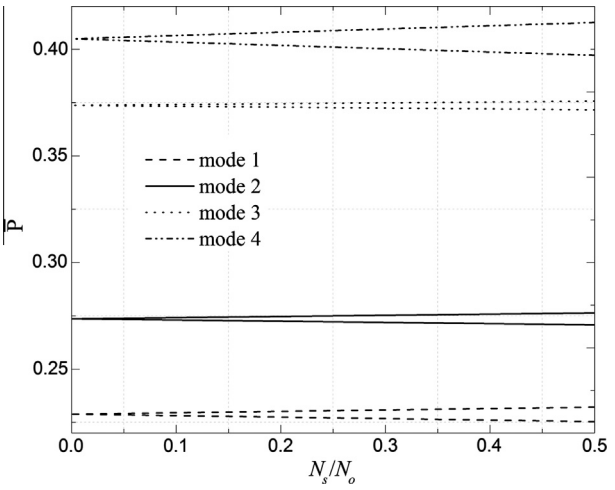

Fig. 24. Unstable regions for the first four modes of FG-V CNTR-FG cylindrical panel with $L/R = 3.0$ under SSSS boundary conditions.

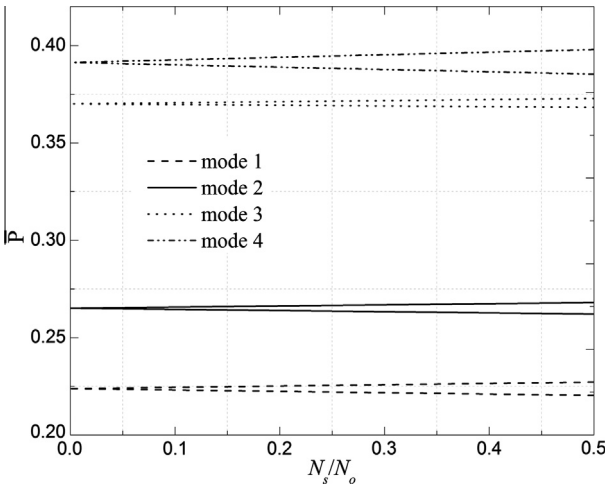

Fig. 25. Unstable regions for the first four modes of FG-O CNTR-FG cylindrical panel with $L/R = 3.0$ under SSSS boundary conditions.

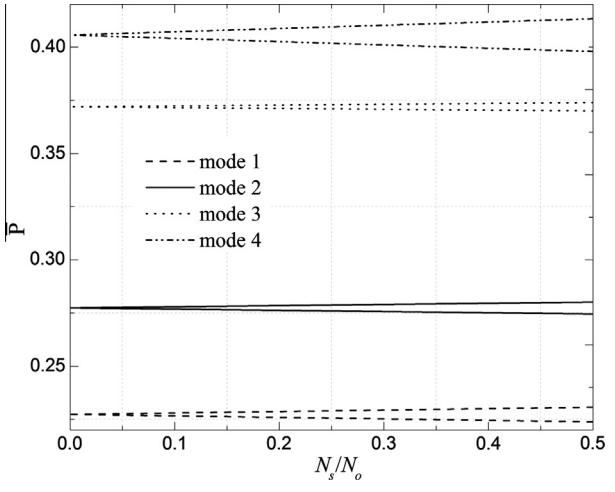

Fig. 26. Unstable regions for the first four modes of FG-X CNTR-FG cylindrical panel with $L/R = 3.0$ under SSSS boundary conditions.

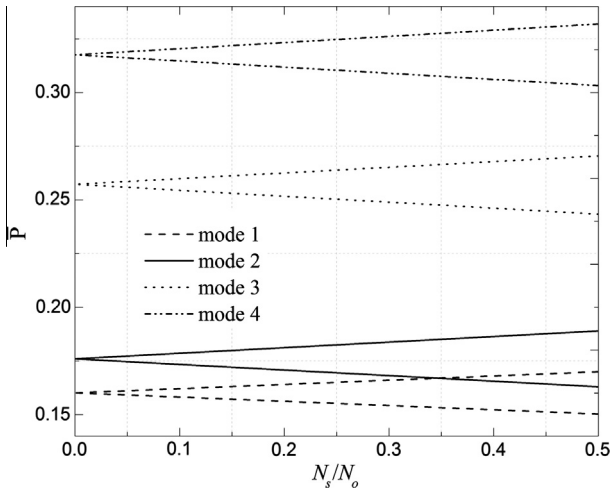

Fig. 27. Unstable regions for the first four modes of UD CNTR-FG cylindrical panel under FFFF boundary conditions (L/R = 1.0, V_{CNT} = 0.14 and R/H = 200).

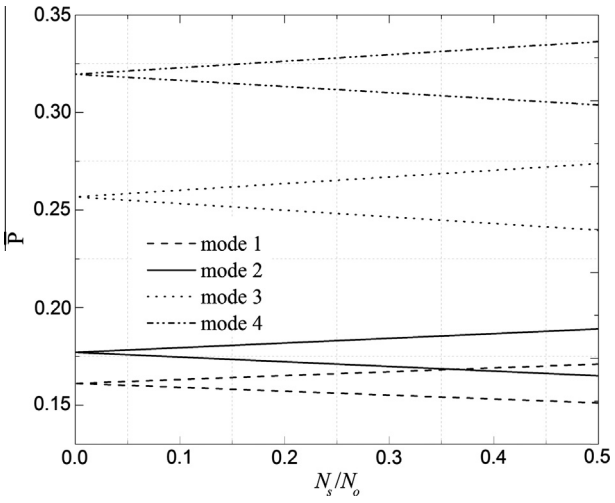

Fig. 28. Unstable regions for the first four modes of FG-V CNTR-FG cylindrical panel under FFFF boundary conditions (L/R = 1.0, V_{CNT} = 0.14 and R/H = 200).

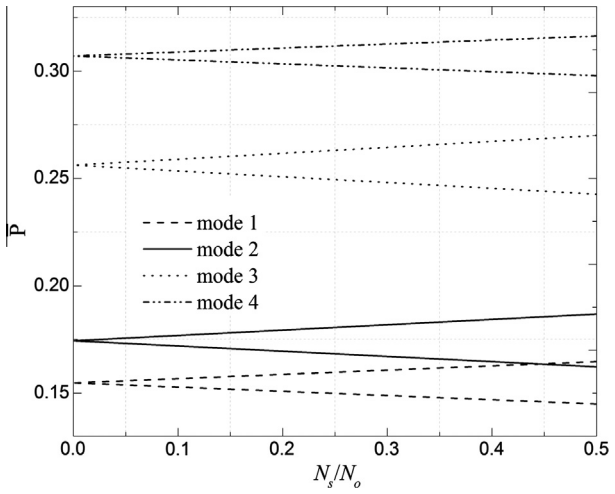

Fig. 29. Unstable regions for the first four modes of FG-O CNTR-FG cylindrical panel under FFFF boundary conditions (L/R = 1.0, V_{CNT} = 0.14 and R/H = 200).

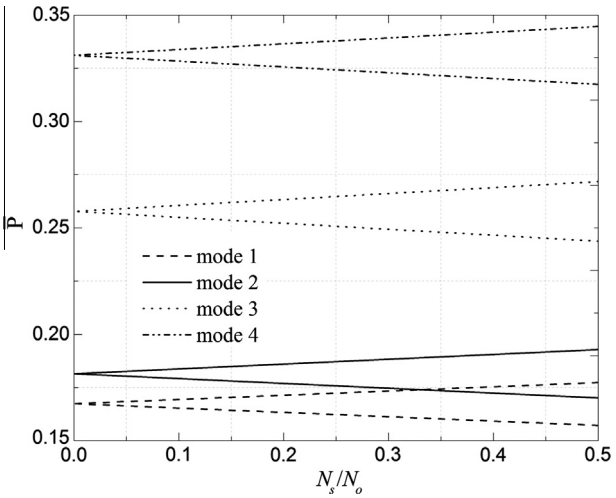

Fig. 30. Unstable regions for the first four modes of FG-X CNTR-FG cylindrical panel under FFFF boundary conditions (L/R = 1.0, V_{CNT} = 0.14 and R/H = 200).

It is also noted that the size of overlapping area for FG-X panel is the largest and that of FG-V panel is the lowest.

Figs. 11–14 show the first four unstable regions of UD, FG-V, FG-O and FG-X CNTR-FG cylindrical panels having CNT volume fraction V_{CNT} = 0.14 under simply supported boundary conditions. The edge-to-radius ratio L/R and the radius-to-thickness ratio R/H is selected as 1.0 and 200, respectively. Comparing the results in Figs. 2 and 5, it can be seen there is no big difference and some similar conclusions can also be derived for the order of the unstable region size and effect about CNT distributions. As CNT volume fraction increases to 0.17, in the first four unstable regions of these four types CNTR-FG cylindrical panels (Figs. 15–18) it can be seen that the change of CNT volume fraction does not affect the responses a lot, but it can also observed that the value of the non-dimensional frequency parameter increases with the increase of CNT volume fraction. That is obvious because CNTR-FG cylindrical panels have larger stiffness when value of CNT volume fraction is larger.

Figs. 19–26 show the first four unstable regions of UD, FG-V, FG-O and FG-X CNTR-FG cylindrical panels having the edge-to-radius ratio, L/R = 2.0 and 3.0 under simply supported boundary conditions. It can be seen that as the edge-to-radius ratio L/R increases to 2.0 and 3.0, the instability region of mode 4 is the widest which is almost twice the other three modes. It can also be seen that the instability regions of modes 1 and 2 are overlapping for CNTR-FG cylindrical panels with L/R = 2.0, while there is no overlapping for CNTR-FG cylindrical panels with L/R = 3.0. In addition to simply supported boundary conditions, Figs. 27–30 show the first four unstable regions of completely free UD, FG-V, FG-O and FG-X CNTR-FG cylindrical panels. The edge-to-radius ratio L/R is chosen to be 1.0. The CNT volume fraction V_{CNT} is selected as 0.14. The radius-to-thickness ratio is assumed to be R/H = 200. It can be seen that there is no big difference between the sizes of unstable regions for the four modes. As N_s/N_0 exceeds 0.34 for UD and FG-V type panels, 0.45 for FG-O type panel and 0.32 for FG-X panel, it can also observed that the instability regions of modes 1 and 2 are overlapping.

5. Conclusions

In this paper, the mesh-free *kp*-Ritz is utilized for dynamic stability analysis of carbon nanotube-reinforced functionally graded (CNTR-FG) cylindrical panels under static and periodic axial force.

The cylindrical panels are reinforced by single-walled carbon nanotubes (SWCNTs) with different types of distributions along thickness direction and effective material properties of the resulting nanocomposite panels are evaluated by Eshelby–Mori–Tanaka approach. A system of Mathieu–Hill equations is obtained via the Ritz minimization procedure and parametric resonance responses are analyzed using Bolotin's method. The 2-D transverse displacement field is approximated by the mesh-free kernel particles estimate. Detailed parametric studies have been carried out and results reveal the influence of volume fraction of carbon nanotubes, edge-to-radius ratio and radius-to-thickness ratio on dynamic stability responses of CNTR-FG cylindrical panels. In addition, effects of different boundary conditions and types of distributions of carbon nanotubes are also examined.

Acknowledgement

The work described in this paper was fully supported by the Grants from the China National Natural Science Foundation (Grant Nos. 11172253 and 51378448).

References

[1] Bolotin VV. The dynamic stability of elastic systems. San Francisco: Holden-Day; 1964.
[2] Vijayaraghavan A, Evan-Iwanowski RM. Parametric instability of circular cylindrical shells. J Appl Mech 1967;34:985–90.
[3] Srinivasan RS, Chellapandi P. Dynamic stability of rectangular laminated composite plates. Compos Struct 1986;24:233–8.
[4] Moorthy J, Reddy JN, Plaut RH. Parametric instability of laminated composite plates with transverse shear deformation. Int J Solids Struct 1990;26:801–11.
[5] Nagai K, Yamaki N. Dynamic stability of circular cylindrical shells under periodic compressive forces. J Sound Vib 1978;58:425–41.
[6] Argento A, Scott RA. Dynamic instability of layered anisotropic circular cylindrical shells, part I: theoretical development. J Sound Vib 1993;162:311–22.
[7] Argento A, Scott RA. Dynamic instability of layered anisotropic circular cylindrical shells, part II: numerical results. J Sound Vib 1993;162:323–32.
[8] Liao CL, Cheng CR. Dynamic stability of stiffened laminated composite plates and shells subjected to in-plane pulsating forces. J Sound Vib 1994;174:335–51.
[9] Ng TY, Lam KY, Reddy JN. Dynamic stability of cross-ply laminated composite cylindrical shells. Int J Mech Sci 1998;40:805–23.
[10] Ganapathi M, Balamurugan V. Dynamic instability analysis of a laminated composite circular cylindrical shell. Compos Struct 1998;69:181–9.
[11] Park SH, Kim JH. Dynamic stability of a completely free circular shell subjected to a follower force. J Sound Vib 2000;231:989–1005.
[12] Yamanouchi M, Koizumi M, Hirai T, Shiota I. In: Proceedings of the first international symposium on functionally gradient materials; 1990. p. 59–64.
[13] Koizumi M. The concept of FGM, ceramic transactions. Funct Gradient Mater 1993;34:3–10.
[14] Zhu P, Lei ZX, Liew KM. Static and free vibration analyses of carbon nanotube-reinforced composite plates using finite element method with first order shear deformation plate theory. Compos Struct 2012;94:1450–60.
[15] Shen HS. Nonlinear bending of functionally graded carbon nanotube-reinforced composite plates in thermal environments. Compos Struct 2009;91:9–19.
[16] Ke LL, Yang J, Kitipornchai S. Nonlinear free vibration of functionally graded carbon nanotube-reinforced composite beams. Compos Struct 2010;92:676–83.
[17] Alibeigloo A. Static analysis of functionally graded carbon nanotube-reinforced composite plate embedded in piezoelectric layers by using theory of elasticity. Compos Struct 2013;95:612–22.
[18] Alibeigloo A, Liew KM. Thermoelastic analysis of functionally graded carbon nanotube-reinforced composite plate using theory of elasticity. Compos Struct 2013;106:873–81.
[19] Lei ZX, Liew KM, Yu JL. Large deflection analysis of functionally graded carbon nanotube-reinforced composite plates by the element-free kp-Ritz method. Comput Meth Appl Mech Eng 2013;256:189–99.
[20] Alibeigloo A. Free vibration analysis of functionally graded carbon nanotube-reinforced composite cylindrical panel embedded in piezoelectric layers by using theory of elasticity. Eur J Mech A/Solid 2014;44:104–15.
[21] Shen HS, Xiang Y. Nonlinear vibration of nanotube-reinforced composite cylindrical shells in thermal environments. Comput Meth Appl Mech Eng 2012;213–216:196–205.
[22] Moradi-Dastjerdi R, Foroutan M, Pourasghar A. Dynamic analysis of functionally graded nanocomposite cylinders reinforced by carbon nanotube by a mesh-free method. Mater Des 2013;44:256–66.
[23] Li X, Gao H, Scrivens WA, Fei D, Xu X, Sutton MA, et al. Reinforcing mechanisms of single-walled carbon nanotube-reinforced polymer composites. J Nanosci Nanotechnol 2007;7:2309–17.
[24] Esawi AMK, Farag MM. Carbon nanotube reinforced composites: potential and current challenges. Mater Des 2007;28:2394–401.
[25] Seidel GD, Lagoudas DC. Micromechanical analysis of the effective elastic properties of carbon nanotube reinforced composites. Mech Mater 2006;38:884–907.
[26] Anumandla V, Gibson RF. A comprehensive closed form micromechanics model for estimating the elastic modulus of nanotube-reinforced composites. Compos Part A 2006;37:2178–85.
[27] Sobhani Aragh B, Nasrollah Barati AH, Hedayati H. Eshelby–Mori–Tanaka approach for vibrational behavior of continuously graded carbon nanotube-reinforced cylindrical panels. Composites Part B 2012;43:1943–54.
[28] Formica G, Lacarbonara W, Alessi R. Vibrations of carbon nanotube-reinforced composites. J Sound Vib 2010;329:1875–89.
[29] Wang J, Pyrz R. Prediction of the overall moduli of layered silicate-reinforced nanocomposites-part I: basic theory and formulas. Compos Sci Technol 2004;64:925–34.
[30] Shen HS. Postbuckling of nanotube-reinforced composite cylindrical shells in thermal environments, part I: axially-loaded shells. Compos Struct 2011;93:2096–108.
[31] Shen HS, Zhang CL. Thermal buckling and postbuckling behavior of functionally graded carbon nanotube-reinforced composite plates. Mater Des 2010;31:3403–11.
[32] Benveniste Y. A new approach to the application of Mori–Tanaka's theory in composite materials. Mech Mater 1987;6:147–57.
[33] Eshelby JD. The determination of the elastic field of an ellipsoidal inclusion, and related problems. Proc Roy Soc London Ser A 1957;241:376–96.
[34] Mura T. Micromechanics of defects in solids. 2nd ed. The Netherlands: Martinus Nijhoff; 1987.
[35] Chen JS, Pan C, Wu CT, Liu WK. Reproducing kernel particle methods for large deformation analysis of non-linear structures. Comput Meth Appl Mech Eng 1996;139:195–227.
[36] Liu WK, Jun S, Zhang YF. Reproducing kernel particle methods. Inter J Numer Meth FL 1995;20:1081–106.
[37] Reddy JN. Applied functional analysis and variational methods in engineering. New York: McGraw-Hill; 1986. reprinted by Krieger, Melbourne, Florida, 1991.
[38] JN R. An introduction to the finite element method. New York: McGraw-Hill; 1993.
[39] Han Y, Elliott J. Molecular dynamics simulations of the elastic properties of polymer/carbon nanotube composites. Comput Mater Sci 2007;39:315–23.
[40] Shen HS, Zhang CL. Thermal buckling and postbuckling behavior of functionally graded carbon nanotube-reinforced composite plates. Mater Des 2010;31:3403–11.
[41] Wang CY, Zhang LC. A critical assessment of the elastic properties and effective wall thickness of single-walled carbon nanotubes. Nanotechnology 2008;19:075075.
[42] Timoshenko SP, JM G. Theory of elastic stability. New York: McGraw-Hill; 1961.
[43] Ng TY, Lam KY, Reddy JN. Dynamic stability of cylindrical panels with transverse shear effects. Int J Solids Struct 1999;36:3483–96.
[44] Lei ZX, Liew KM, Yu JL. Buckling analysis of functionally graded carbon nanotube-reinforced composite plates using the element-free kp-Ritz method. Compos Struct 2013;98:160–8.
[45] Liew KM, Lei ZX, Yu JL, Zhang LW. Postbuckling of carbon nanotube-reinforced functionally graded cylindrical panels under axial compression using a meshless approach. Comput Meth Appl Mech Eng 2014;268:1–17.
[46] Zhang LW, Lei ZX, Liew KM, Yu JL. Static and dynamic of carbon nanotube reinforced functionally graded cylindrical panels. Compos Struct 2014;111:205–12.
[47] Zhang LW, Lei ZX, Liew KM, Yu JL. Large deflection geometrically nonlinear analysis of carbon nanotube-reinforced functionally graded cylindrical panels. Comput Meth Appl Mech Eng 2014;273:1–18.